Deep-sea fragmentation style of Havre revealed by dendrogrammatic analyses of particle morphometry

Authors: T. Dürig[1,2]*, J.D.L. White[1], B. Zimanowski[3], R. Büttner[3], A. Murch[1,4] and R.J. Carey[5]

Affiliations:

[1]Geology Department, University of Otago, New Zealand.

[2]Institute of Earth Sciences, University of Iceland, Iceland.

[3]Physikalisch Vulkanologisches Labor, Universität Würzburg, Germany.

[4]National Museum of Nature and Science, Tokyo, Japan.

[5]School of Natural Sciences, University of Tasmania, Australia.

*tobi@hi.is

Abstract

In 2012, the eruption of deep-sea volcano Havre produced an abundance of fine ash at a depth of ~1000 m below sea level. In this study the 2D shapes of Havre ash grains retrieved from the seafloor were compared quantitatively with those of particles generated in a suite of different fragmentation experiments, which used remelted rhyolitic rock and pumice from the eruption site. A new statistical data analysis technique, denoted Dendrogrammatic Analysis of Particle Morphology (DAPM) is introduced. It is designed to compare large numbers of morphometric data sets containing shape information for a set of ash particles, to group them by morphological similarities and to visualize these clusters in a dendrogram. Further steps involve t-tests and equivalence tests and reveal morphometric differences as well as matching features. The DAPM suggests that the majority of Havre ash was thermohydraulically produced by induced fuel coolant-interaction. A subset of ash particles feature an elongate tube morphology. Their morphometry matches that of particles that were experimentally produced by a combination of shearing and quenching, and we infer that the natural particles were formed by synextrusive ash-venting.

Key words

Particle shape analysis, volcanic ash, Havre seamount, induced fuel-coolant interaction, fragmentation mechanisms

Introduction

Juvenile pyroclasts are generated by fragmentation processes in which mechanical stresses cause local material failure and drive the propagation of cracks through magma (e.g., Papale 1999; Zhang 1999; Zimanowski et al. 2003; Dürig et al. 2012c). The sources and dynamics of mechanical stress vary with eruptive style (e.g., Heiken and Wohletz 1985; Büttner et al. 1999; Dürig et al. 2012b; Murtagh and White 2013; Leibrandt and Le Pennec 2015; White and Valentine 2016; Schmith et al. 2017). During pumice-forming explosive eruptions subaerial fragmentation is generally considered the result of strain induced by rapid magma ascent or decompression (Gonnermann 2015; Cashman and Scheu 2015). Other ash generation processes include fragmentation during fuel-coolant interaction of magma with water, when stress is exerted on a magmatic melt by rapidly expanding pockets of thermally expanding water (Zimanowski et al. 2015; Dürig et al. 2020). As a result, at the interface between magma and water shock waves are generated, which rush through the melt with super-sonic speed, strongly affecting its fracture-mechanical properties (Wohletz 1986; Büttner and Zimanowski 1998; Dürig et al. 2012c; Wohletz et al. 2013). Furthermore, the rapid increase of thermohydraulic stress leads to an acceleration of cracks, which when reaching a stability threshold produce uneven fracture surfaces and finally bifurcate (Dürig and Zimanowski 2012). Consequently, "active" phreatomagmatic particles originating from the magma water interface are characterized by distinct features such as a blocky shape, conchoidal fractures and stepped surfaces (Büttner and Zimanowski 1998; Büttner et al. 1999, 2002; Fitch and Fagents 2020) that reflect both shock-waves and crack bifurcation (Dürig et al. 2012b).

Interpretation of fragmentation processes from analysis of particle morphology is complicated by the fact that fragmentation processes are also influenced by factors such as magma heterogeneity (i.e., crystallinity and vesicularity), stress geometry, and pre-existing stresses, e.g., due to thermal quenching (Dürig and Zimanowski 2012). Moreover, secondary processes can alter pyroclasts, due to transport, abrasion or secondary thermal granulation (Cashman and Scheu 2015).

Volcanic juvenile pyroclasts are, however, often the only "eye witnesses" of eruptive processes, and their morphology is frequently used to infer eruptive styles (e.g., Heiken and Wohletz 1985; Büttner et al. 1999, 2002; Murtagh and White 2013; Schipper et al. 2013b; Iverson et al. 2014; Leibrandt and Le Pennec 2015; Schmith et al. 2017; Avery et al. 2017). Primary particle shapes can shed light on details of eruption dynamics (e.g., Yamanoi et al. 2008; Andronico et al. 2009; Wright et al. 2012; Suzuki et al. 2013; Miwa et al. 2013, 2015; Eychenne et al. 2015; Gurioli et al. 2015), while modifications to primary particle shape are further used to explore modes of transport, dispersal and emplacement (e.g., Taddeucci and Palladino 2002; Riley et al. 2003; Maria and Carey 2007; Durant et al. 2009; Mele et al. 2011; Klawonn et al. 2014; Dioguardi et al. 2017).

The qualitative morphological description and interpretation of juvenile pyroclasts has a long history in volcanology, beginning with inferences from shapes of volcanic bombs (Scrope 1858; Gilbert 1890). Qualitative analyses for smaller ash grains began in earnest with published galleries of scanning electron microscope (SEM) images from ash particles, sorted by (known) eruptive style (Heiken 1972, 1974; Heiken and Wohletz 1985). More recently, interpreter-independent methods have been applied using dimensionless descriptors to characterize the two-dimensional shape of either projected silhouettes (e.g., Dellino and La

Volpe 1996; Coltelli et al. 2008; Mele et al. 2015, 2011; Lautze et al. 2012, 2013; Iverson et al. 2014; Cioni et al. 2014; Leibrandt and Le Pennec 2015; Alvarado et al. 2016; Schmith et al. 2017; Avery et al. 2017) or cross-sections (e.g., Cannata et al. 2014; Liu et al. 2015a, b; Verolino et al. 2019) of ash or lapilli samples in two dimensions. Despite the extensive work on shape analysis conducted by numerous groups, comparability of published results remains limited, and no consensus has yet been reached regarding which set of shape parameters best describes particle's silhouettes or cross-sections. Open source software PARTIcle Shape ANalyzer (PARTISAN) published to help address this issue (Dürig et al. 2018) computes 23 dimensionless shape parameters of binarized 2D objects according to the five morphometric schemes most commonly used in volcanology (Dellino and La Volpe 1996; Cioni et al. 2014; Leibrandt and Le Pennec 2015; Liu et al. 2015b; Schmith et al. 2017). Based on M selected shape parameters, the morphometric profile of a sample with N particles can then be expressed by a matrix of $N \times M$ shape parameter values. Such a matrix is in this paper denoted as a "morphometric data set". Morphometric data sets are often used in experimental volcanology to compare multiple samples with one another, to investigate their morphological differences, to see which samples group together, and to determine which of the experimentally produced particles match best with natural ash samples. Such investigations often involve a large number of statistical comparisons and must deal with a number of mathematical pitfalls (see section "Statistical methods used for morphometric analysis").

We present here a newly developed statistical procedure for multiple morphometric particle analyses, which we call "dendrogrammatic analysis of particle morphometry (DAPM)". It enables the user to construct diagrams that allow sorting of morphometric data sets, and identification of samples that are significantly different from one another, as well as those of similar shapes.

To demonstrate the potential of this approach, we used the deep-sea 2012 eruption of Havre volcano as a test case: pristine 3-year old volcanic ash particles from that eruption were compared morphometrically with particles of the same grain size fraction generated in a series of experiments using the original Havre rhyolite. The experiments were tailored to reproduce potential fragmentation mechanisms relevant in a deep submarine setting. The statistical results support findings from a previous study (Dürig et al. 2020), showing that explosive thermohydraulic ash generation by Induced Fuel Coolant Interaction (IFCI) may have been a dominant process during the Havre 2012 eruption.

Havre: geological setting

Havre is a silicic submarine volcano situated in the Kermadec arc, north of New Zealand. Its 2012 eruption of rhyolite produced lava flows from 14 vents located in the south-western quadrant of the caldera (Carey et al. 2018). It also formed a pumice raft of ~400 km^2 (Jutzeler et al. 2014; Carey et al. 2018; Manga et al. 2018), a layer of > 1 m diameter pumice blocks on the seafloor, denoted "giant pumice" (Fauria and Manga 2018; Carey et al. 2018; Manga et al. 2018), an ash-lapilli-block deposit and a layer dominated by ash smaller than 125 µm (Ash and Lapilli unit, Murch et al. 2019b), which we refer to as "fine ash". In a 2015 voyage investigating the Havre eruption deposits, an area of over 35 km^2 was mapped with remotely operated and autonomous vehicles (Carey et al. 2018). The Ash with Lapilli deposit is >0.1 km^3 and shows no consistent thinning or fining trends, implying that a large proportion of erupted ash extends beyond the mapped area (Murch et al. 2019b).

Natural volcanic ash samples

For this study, we analyzed glassy ash particles from six samples collected near the eruption site at a depth of 900 - 1100 m below sea level by the *Jason* remotely operated vehicle, labelled according to their location of retrieval “Nat1” to “Nat6” (Fig.1). While “Nat1” through “Nat4” were collected by push core, a vacuum-like “slurp” sampler was used for sampling “Nat5” and “Nat6”. Filters were applied to retain the fine ash (for details, see Supplemental material in Murch et al. 2019b). Although the tephra samples were collected by different methods, a comparison between the grain size peaks of all the different samples collected at Havre showed there is no real consistent difference between them (Murch et al. 2019b). The samples contain with up to 90 wt% (Murch et al. 2019b) a large proportion of ash finer than 125 µm, of which 50 to 80 wt% is characterized by blocky, curvi-planar shapes, low vesicularity and stepped surfaces (Murch et al. 2019b, a). Four curvi-planar grains are presented in Figure 2 (a-d). Other morphological classes identified comprise grains with angular, elongate-tube and fluidal features following the classification scheme of Murch et al. (2019b, 2020). Angular grains (Fig. 2 e-h) feature characteristic concavities formed by brittle-fractured vesicle walls, whereas elongate-tube grains are characterized by their elongated shapes and tubular vesicles (Fig. 2 i-l). Fluidal grains show flowing or molten surfaces, with features characteristic for ductile deformation processes (Murch et al. 2019a). Table 1 lists the composition of each sample by morphological class.

While a previous study focused exclusively on curvi-planar Havre ash, separated by location (Dürig et al. 2020), here a different approach was chosen. Based on previous findings (Murch et al. 2019b, 2020; Dürig et al. 2020) we can assume that each morphological class reflects a specific fragmentation mechanism. The numbers of particles for each class and sample are, however, quite variable, ranging from 1 to 74 (see Table 1). Having such large variances is not a preferred condition when applying comparative multivariate statistical tests, such as t-tests or ANOVA, because strongly unequal sample sizes might introduce additional uncertainties (Ahad and Yahaya 2014; Blanca et al. 2017). To overcome this issue, data from “Nat1” to “Nat6” were combined to form one large sample. The particles of this sample were then binned by morphological class, yielding binned subsamples of 247 curvi-planar, 163 angular, 59 elongate tube and 26 fluidal grains (see Table 1). This procedure is appropriate for examining processes of fragmentation at the vent, but precludes here any site-by-site evaluation of samples.

For the curvi-planar and angular class, the morphologically binned samples were subsequently split into data sets of roughly comparable size (of at least ~50) by using a random number generator and assigning an arbitrary number (ranging from 1 to 4 for curvi-planar grains, and from 1 to 3 for angular grains, respectively) to each particle.

This approach allows us to statistically analyze angular and elongate-tube particle samples, as well as blocky, curvi-planar ones. The following binned data sets were obtained (Fig. 2):

- four binned samples with curvi-planar grains, labelled “NatIcp”, “NatIIcp”, “NatIIIcp” and “NatIVcp”
- three binned samples with angular grains, denoted “NatIang”, “NatIIang” and “NatIIIang”
- one binned sample with 59 elongate-tube grains, denoted “NatItub”

The sample size for fluidal particles (26) was deemed insufficient, and this morphological class was excluded from further statistical analyses.

Experiments

In order to study ash-forming fragmentation mechanisms potentially relevant to Havre volcano, fragmentation experiments of remelted Havre rhyolite were conducted under laboratory conditions.

For all melt fragmentation experiments discussed in this study, 250 g of raw Havre material was crushed and remelted under non-equilibrium conditions in a 10 cm diameter cylindrical steel crucible. Starting material was either pumice ("P", sample location see Fig. 1) or rhyolitic dome rock ("R", see Fig.1). The melt was inductively heated to 1573 K and then kept at this temperature for 30 minutes to equilibrate. It was then slowly cooled over a 30-minute period to the experimental temperature of 1423 K. During the whole period, the crucible was covered by a lid, which was removed only seconds before the experiment.

Four types of melt fragmentation experiments were conducted:

"Dry runs" (identifier: "dry"): These fragmentation experiments followed standardized procedures used to test material-specific fragmentation thresholds of magmatic melts (Büttner et al. 2006; Dürig et al. 2012a). The melt inside the crucible was overloaded by mechanical stress generated by injecting pressurized argon at 8.5 MPa from below. When being subjected to the expanding gas, the cylindrical plug was deformed until it failed in a brittle way, resulting in the kinetic release of melt fragments. Since these runs mechanically fragment melt quasi-isothermally with applied stress, they are also known as "stress-induced fragmentation experiments" (Büttner et al. 2006). The resulting particles are analogues for products of magmatic fragmentation (Büttner et al. 2006; Dürig et al. 2012a). Either pumice or dome rock were used as starting material for dry runs.

"IFCI runs" (identifier "ifci"): The setup is the same as for dry runs, but with an added hosepipe leading to the top of the crucible (Austin-Erickson et al. 2008; Dürig et al. 2020). Two seconds before stress generation (i.e., gas injection), 240 ml of water was added from above forming a water layer on top of the melt. At the onset of fragmentation driven by the expanding Argon gas, water entered the opening cracks and initiated downward-advancing IFCI that thermo-hydraulically "boosted" fragmentation (Dürig et al. 2020). Thus, fragments were produced by (1) dry quasi-isothermal stress-induced cracking, and (2) thermohydraulic processes during IFCI. These "IFCI particles" were thus much more abundant at the leading edge of the ejected cloud of fragments than in the following ejecta (Dürig et al. 2020). As for dry runs, raw material for the melt was either pumice or dome rock.

"Granulation runs" (identifier "gra"): Thermal granulation occurs when hot melt is put into contact with considerable volumes of water. When facing the coolant, the melt forms a crust, while contracting, thus generating mechanical "quenching" stress between the solidifying outer crust and the (hot) interior (e.g., Chadwick et al. 2008; Schipper et al. 2013b; Cas and Giordano 2014; van Otterloo et al. 2015; White et al. 2015; Cas and Simmons 2018). In our granulation runs the melt was extruded from the crucible using a ceramic scraper (due to the high viscosity of the rhyolitic Havre material), then dropped into a calorimeter filled with 5 liters of water. As a result, the extruded melt was stretched and pre-stressed before being submerged into the water. As a result the melt fragments, with cracks being driven by a combination of mechanical pre-stresses and (contractional) quenching stress. These runs were conducted either with remelted pumice or with dome rocks.

“Crucible contraction runs” with dynamo-thermal fragmentation (identifier “con”): For these runs, dome rock was crushed and remelted. The melt formed a plug which was kept inside the crucible and cooled down to room temperature in free air, with no lid. During cooling, the steel crucible contracted faster than the solidifying melt and exerted a radial compressional pressure on it. This fragmented the plug. The resulting samples are hence products of a thermo-mechanical fragmentation, such as occurs when brittle crusts are fragmented by continued lava movement (White 2000), or due to compressional stress exerted on the crust of a rapidly cooling lava body.

In addition to melt fragmentation experiments, **abrasion** (identifier “abr”) caused by the collisional breakup of pumice blocks was simulated by rubbing two pieces of pumice against each other, while pushing them together with constant force, and collecting the resulting particles.

Dry and IFCI runs were conducted in two configurations:

- “open runs”, in which generated fragments were ejected into free air, ballistically transported and deposited across the experimental area. A part of the ejecta was collected in a bowl containing 600 ml of deionized water, which had been placed 30 cm from the crucible.
- “U-tube runs”, for which a 10 cm-diameter U-shaped steel tube was mounted with one opening placed a few centimeters above the crucible orifice. The other end led to a 600 ml bowl of deionized water. In these runs, small particles (plus water and steam in case of IFCI runs) of the leading ejecta front were guided into the water bowl. The tube remained fixed until larger fragments of the following ejecta entered it (typically, ~30 ms after fragmentation began), pushing the U-tube upward and removing it from the particle-ejection path. Fragments ejected after U-tube separation followed free ballistic trajectories and were deposited across the whole experimental area (Dürig et al. 2020).

To study the potential influence of post-fragmentation cooling processes on the morphology of particles, experimental particles were retrieved at different sampling locations:

- **G**: "Ground" samples; ballistically transported particles generated in open runs and deposited on the floor were retrieved using a vacuum cleaner with micro-porous paper bags
- **B**: "Bowl" samples; ballistically transported fragments, which were generated in open runs and deposited in the water bowl were sampled by using paper filters.
- **W**: "Wet" samples; particles from open IFCI runs, which were deposited inside microscopic water droplets on the ceiling and walls (Dürig et al. 2020), were collected using paper tissues.

- **U**: "U-tube" samples; particles generated in U-tube runs, which were injected through the U-tube into water and retrieved inside the water bowl.
- **M**: "Calorimeter" samples, generated in thermal granulation runs were sampled inside a water-filled calorimeter.
- **C**: "Contraction" samples; particles generated in crucible contraction runs were retrieved inside the crucible.

In total, 14 different experimental samples were analyzed and compared with the eight natural ash samples.

Figure 3 presents SEM images of experimental grains from each sample. The notation of the experimental samples is illustrated in Figure 4.

Particle shape parametrization

All particles collected were sieved at 1 Φ steps, with Φ being related to the grainsize s (in mm) by $s = 2^{-\Phi}$. For all morphometrical analyses the 4 Φ fraction was used, i.e. grains smaller than 125 µm and bigger than 63 µm. The particles were randomly selected and mounted on carbon-coated tape, spaced to avoid grain-grain contacts. Backscatter electron scans were produced at a resolution of 2048 x 1536 pixels with a Zeiss Sigma VP FEG scanning electron microscope (SEM). On average, the imaged particles had an area of ~20,200 pixels.

Next, each particle was segmented and binarized, resulting in a black and white image showing the projected area of the particle towards the underlying plane. Since our aim was to to analyze signatures of fragmentation processes, during this step, grains with morphologies that we considered dominated by the presence of phenocrysts (obvious straight edges) or microcrystals (outlines with apparent straight-edged protrusions or embayments) were omitted. The rate of omitted grains was less than 1% for the samples Nat1, Nat3 and Nat5, ~ 5% for sample Nat6, but up to 20% for the samples Nat2 and Nat4. The latter were closest to the dome (Fig. 1), an area which is known to be covered by microlite-rich grains, which probably originate from the collapsing or fragmenting dome itself (Ikegami et al. 2018; Carey et al. 2018; Manga et al. 2018).

These binarized images were used as input data for the software PARTISAN (Dürig et al. 2018). This program quantifies shapes of silhouette outlines, based on 5 morphometric systems (Dellino and La Volpe 1996; Cioni et al. 2014; Leibrandt and Le Pennec 2015; Liu et al. 2015b; Schmith et al. 2017), and computes 23 dimensionless shape parameters. Several of them are identical throughout the various systems (see Table 2 in Dürig et al. 2018), leaving a set of 18 non-identical shape parameters (see Table 2 and Fig. 5).

Statistical methods used for morphometric analysis

For all types of statistical tests, a level of significance α of 5% was selected.

T-tests

In order to verify significant differences between two morphometric data sets, two-tailed t-tests were applied, using the software SPSS (IBM Corp. 2017). A t-test is a statistical method based on the Student's t-distribution (Student 1908; Zabell 2008) that has been applied in previous analyses of particle shape (Dellino et al. 2001; Dürig et al. 2012b; Schipper et al. 2013b; Jordan et al. 2014). It provides the error likelihood ("*p*-value") of the null hypothesis, which states that the two tested data sets are from the same population. If the error likelihood p is below the level of significance α, the null hypothesis can be rejected: the data sets are then verified to be “significantly different” in the tested hypothesis (Brosius 1998; Dürig et al. 2012b).

Before a t-test is applied, there must be a test to assess whether the variances of the data sets are homogeneous (i.e., the same within a narrow tolerance), and we used a Levene-test (IBM Corp. 2017). In cases where the variances of the compared data sets are verified to be homogeneous, the results of a “pooled variance t-test” (Brosius 1998) can be trusted. If this precondition is not met, however, the better choice is a “separated variance t-test”, developed by Welch (1947).

While a t-test is a very robust and reliable method to test two sets of randomly selected samples, its reliability decreases when the same data sets are repeatedly used (Bender and Lange 2001). In such cases the likelihood of a type I error (i.e., the test indicates a significant difference where there is none) increases. There are post-hoc adjustments which could counter this effect, e.g. the Bonferroni correction (Bonferroni 1936), but these adjustments are inevitably done at the price of decreasing the statistical power (Perneger 1998; Bender and Lange 2001). In other words, applying a post-hoc correction increases the likelihood of type II errors, where genuine differences are no longer detected by the test.

One-way analysis of variances (ANOVA)

The same difficulty applies to a statistical method very similar to t-tests we applied in our study, the one-way analysis of variances (ANOVA). In contrast to t-tests, ANOVA is based on the F-distribution and is designed to be applied to more than two data sets at once (Brosius 1998). As for t-tests, post-hoc corrections have to be applied to adjust for the above described effect. For example, an inter-comparison of 22 samples with each other would require $21*22/2 = 231$ tests, and each sample would be tested 21 times. We therefore applied ANOVA with post-hoc corrections using SPSS, whenever data sets were repeatedly tested.

Levene-tests were again performed before each test to check if the variances of the data sets were homogeneous. Then, depending on the outcome of the Levene-tests, the p-values were computed via ANOVA, with subsequent application of the Tukey’s range test (also known as Tukey honestly significant difference HSD) as post-hoc correction for assumed homogeneous variances (Tukey 1949), or of a Games-Howell post-hoc adjustment (Games et al. 1979) for heterogeneous variances.

Equivalence tests (“e-tests”)

It is notable that while both ANOVA and t-tests are useful for proving significant differences, failing these tests alone can, from a mathematical point of view, not be used as proof for equivalence (Walker and Nowacki 2011; Dürig et al. 2012b). In order to verify that two data sets are in fact “statistically equivalent” in the tested shape parameters, equivalence tests (“e-tests”) were applied. For image particle analysis, this method was introduced by Dürig et al. (2012b) and tests whether the confidence interval C (with level of significance being α) of a shape parameter from one sample is within a given range D_{max}. The latter parameter is known as “maximum difference range” (Dürig et al. 2012b) or as the “equivalence margin”. It determines the maximum “acceptable” difference from the mean of the compared shape parameter (Rasch and Guiard 2004; Wellek 2010). For mathematical details on this method, the reader is referred to Dürig et al. (2012b). Importantly, e-tests are based on the pooled

Student's t-function and thus only provide reliable results for data sets of homogeneous variances. It is hence necessary to check if this pre-condition is met. In this study this was done by additional F-tests (Nelson 2008). Since at this point the variances have already been tested with Levene-tests, this step is optional. E-test results based on data sets with heterogeneous variances were omitted.

In order to determine D_{max}, benchmark tests were conducted by applying e-tests to all data sets of natural ash samples (Nat1 to Nat6) with data size 20 and larger, separated by morphological class. Five and four sample subsets (marked with asterisk in Table 1) were used to find the equivalence margin for curvi-planar grains D_{max_cp} and for angular grains D_{max_ang}, respectively.

For these calibration tests it is assumed that all data sets of the same morphological class originate from the same particle population and hence were generated by the same mechanism. The applied procedure was as follows: for each shape parameter the values for the respective equivalence margin D_{max} started at 0.01 and was increased stepwise by 0.01, until the e-test indicated a statistical equivalence. It should be noted that due to the necessary precondition of homogeneity of variances, not every e-test yielded results for each of the tested shape parameters.

The results for D_{max_cp} and D_{max_ang} are listed in Table 2. The values specify the "natural spread" within the respective shape parameter and were therefore used as morphological class-specific equivalence margins. Since insufficient data were available for elongate-tube particles, e-tests with samples of this morphological class were conducted by using both D_{max_cp} and D_{max_ang} as equivalence margins instead.

Distance matrix X and construction of morphometric particle dendrograms

The objective and mathematical challenge of this study was to compare 22 samples across 18 parameters and find a way to sort the data sets according to their respective statistical "dissimilarity".

For this purpose, the ANOVA-based *p*-values were processed for all 18 shape parameters and *n* tested samples to construct a distance matrix *X*, with p_{ijk} being the *p*-value of data set *i* tested with the one from data set *j* in the k-th shape parameter:

$$X_{ij} = \sum_{k=1}^{18} Y_{ijk} \quad (1)$$

with Y_{ijk} being defined as:

$$Y_{ijk} = \begin{cases} log\left(1 + \frac{1}{p_{ijk}}\right) & if\ p_{ijk} < 0.05 \\ 0 & if\ p_{ijk} \geq 0.05 \end{cases} \quad (2)$$

We note that for Y_{ijk}, only the *p*-values for significantly different shape parameters are considered. According to eq. (1) and (2), very low *p*-values, implying a high likelihood for differences in the tested shape parameter, would result in very large values for X_{ij}. The latter quantity can hence be used as a measure of morphometric difference between sample *i* and sample *j*. Here, we suggest the use of a logarithm rather than the pure reciprocal *p*-value, in order to get manageable values as a measure for difference. The reciprocal *p*-value is increased by 1 in order to avoid negative numbers.

By using the software R, dendrograms were drawn by using X as distance matrices in complete linkage. These morphometric particle dendrograms present visually the relative morphometric differences between the samples tested by grouping them in clusters. The y-axis represents the morphometric differences between the samples and is labeled “dissimilarity”.

The dendrogrammatic analysis of particle morphometry (DAPM)

As pointed out above the statistical power of these tests is low if a large number of samples are compared with each other. This means that in such cases samples that are grouped next to each other with a dissimilarity of 0 do not necessarily have to be statistically equivalent. The zero difference may simply reflect limits to the statistical power of the underlying ANOVA in resolving genuine difference in the shape parameters. It is, however, safe to accept that samples that are grouped apart from each other in the morphometric dendrogram (separated by a dissimilarity values >0) are verified as significantly different. This leads us to the following multi-step strategy:

1. First, the ANOVA-based matrix X is computed by comparing all samples (in our case 22), resulting in a “level 1” dendrogram. This preliminary diagram is mainly used for pre-sorting and allows us to identify the main morphometric clusters.
2. The dendrogram approach is then applied, focusing exclusively on individual clusters. This way, with a lower number of samples compared, and the statistical power of the ANOVA increased, further morphometric differences of the samples in the analyzed cluster can be detected. As a consequence, the resulting morphometric “level 2” dendrograms might split the samples further into sub-clusters.
3. This procedure is repeated for each sub-cluster (and by stepwise increasing the “levels”), until no further cluster separation is achieved. In the presented example, none of the sub-clusters showed further diversification at levels larger than two.
4. Samples that are at highest level still grouped together with a dissimilarity of 0 are then treated as potential candidates for being of “statistically equivalent morphometry”. They are further analyzed in all 18 shape parameters by applying additional two-tailed t-tests without post-hoc correction. This approach guarantees a high statistical power and a low likelihood of type II errors.
5. As a final step, for samples for which no significant differences were found by t-tests in any of the shape parameters, morphometric equivalence was verified by e-tests using the threshold values D_{max} listed in Table 2 as equivalence margins.

Results

Figure 6 presents the resulting “level 1” dendrogram, which is based on ANOVA for all 22 data sets. The data sets can be grouped into four main clusters (labelled “cluster1” … “cluster4”) of relatively low dissimilarity, indicating a certain degree of similarity in their morphometric characteristics.

Cluster1

In addition to natural elongate-tube ash (NatItub), cluster1 comprises experimental samples from remelted dome rock, resulting from granulation runs with ductiley deformed and pre-stressed melt (RgraM), dynamo-thermal crucible contraction runs (RconC), and from dry fragmentation and subsequent ballistic transportation into water (RdryB). Figure 7 shows the resulting “level 2” dendrogram for cluster 1. The increased statistical power of the ANOVA leads to a clear separation of some of the analyzed samples. RdryB and RconM were verified to be of unique morphometry, and both are significantly different to RgraM and NatItub. The dendrogram groups the latter two samples together with a dissimilarity of 0. T-tests do not reveal any significant differences between them in any of the tested shape parameters.

Table 3 lists the minimum range *D*, under which the e-tests between RgraM and NatItub are passed. Because we lacked equivalence margins that are specifically calibrated for elongate-tube class particles, D_{max_cp} and D_{max_ang} were used instead. Since for all tested shape parameters the pre-condition of homogeneity of variances was verified by F-tests, and the values of *D* do not exceed any of the thresholds (in fact *D* even appears to be considerably smaller), NatItub and RgraM are proven to be statistically equivalent within the suggested equivalence margins.

Cluster2

Cluster2 is composed of samples from IFCI experiments with remelted pumice (PifciU, PifciW), from pumice-based granulation runs with ductiley deformed and pre-stressed melt (PgraM), from IFCI runs with remelted dome-rock which were ballistically transported and deposited on the floor (RifciG) and into water (RifciB).

The “level 2” dendrogram for cluster2 (Fig. 8) shows PgraM separated from the rest of the samples.

Equivalence tests using D_{max_cp} and D_{max_ang} reveal a statistical equivalence between RifciG and RifciB and between PifciU and PifciW for 14/18 and 13/18 shape parameters, respectively (see Table 3). (No statement can be made for the equivalence of the remaining shape parameters, since their variances were not homogeneous.)

While RifciG/B and PifciU/W can be grouped together, comparisons between these two pairs by additional t-tests reveal significant differences in some of the shape parameters (see Table 4). This suggests that RifciG/B and PifciU/W form two subclusters.

Cluster3

The largest morphometric cluster is formed by cluster3, which groups the four natural curvi-planar ash samples together with no less than five of the experimental samples. “Level 2” ANOVA for the samples of cluster3 results in a refined dendrogram, which divides the samples into three sub-groups (see Fig. 9). One sub-cluster consists of PdryG and RdryG, for which t-tests reveal significant differences in 7 of the 18 shape parameters (see Table 4).

The biggest sub-cluster comprises the curvi-planar ash samples NatIcp – NatIVcp, together with RifciU and RifciW. T-tests (e.g., see Table 4) show no significant differences between the shape parameters of these samples, and e-tests verify a statistical equivalence between the natural curvi-planar ash and the experimental samples RifciU and RifciW (see Table 5).

In contrast to RifciU and RifciW, sample RdryU is characterized by a small but measurable degree of dissimilarity towards the natural curvi-planar ash samples, thus forming a “subcluster” by its own.

Cluster4

Cluster4 is composed of the natural angular ash samples (NatIang, NatIIang and NatIIIIang) and the experimental particles resulting from abrasion experiments (PabrG). According to the "level 1" dendrogram (Fig. 6), experimental and natural grains of this group show slight but discernible differences, indicated by a relatively small dissimilarity value.

Figure 10 illustrates the merged findings, based on "level 1" and "level 2" dendrograms and the results from t-tests and e-tests. This (semi-quantitative) fan dendrogram serves as basis for the subsequent discussion.

Discussion

The DAPM groups the natural ash samples of known equivalent shape (NatIang…NatIIIang; NatIcp…NatIVcp) correctly together (Fig. 10). Furthermore, the tested method is evidently capable of discriminating the samples by their morphological classes, forming three different morphometric clusters. This demonstrates the potential for automated morphological classification, a task which so far has had to rely on time-consuming "manual" counting (Murch et al. 2019b, 2020).

U-tube particles and particles retrieved in water droplets are found to be grouped together in pairs of statistically equivalent morphology (RifciU/W; PifciU/W). This is in agreement with the findings of a previous study (Dürig et al. 2020), according to which IFCI particles are transported with the leading ejecta front and deposited within droplets in the vicinity of the artificial conduit. This explains why RifciU is identical to RifciW (and so is PifciU to PifciW).

RifciU and RifciW originate from IFCI experiments with remelted dome rock, which reproduced particles that are of statistically equivalent morphometry with natural curvi-planar ash. Also this result is consistent with the conclusions of Dürig et al. (2020), where four experimental samples (RifciU, RifciW, RifciG and RdryG) were compared with curvi-planar natural ash via t-tests and e-tests. That work was based on the same SEM images but used differently arranged data sets for the natural curvi-planar ash (separated by Nat1 – Nat6). The DAPM results presented here, which are based on a significantly increased sample set, corroborate the inferences of Dürig et al. (2020) according to which induced fuel-coolant interaction was the dominant ash generation mechanism for the Havre 2012 eruption and responsible for the production of curvi-planar ash particles. An additional inference that can be made from the similarity with lab particles, is that the curvi-planar ash appears to be from magma that did not have vesicles with sufficiently close spacing to play a significant role in determining particle shape.

Moreover, we infer from the verified statistical morphometric equivalence of RgraM with NatItub that the natural ash particles of elongate-tube morphological class were generated by processes reproduced by granulation runs with ductiley deformed and pre-stressed melt. These results corroborate the inference of Murch et al. (2020), who suggested a syn-extrusive ash venting scenario, in which sheared lava was fragmented and the clasts erupted through a system of narrow cracks/fissures. Strong shearing produced elongate vesicles and high magma permeability, and fragments of this sheared magma were then quenched as they entered the water column. Syn-extrusive ash venting has been linked to elongate tube shaped particles before, in a study on Cordon Caulle (Chile), though those grains were produced under subaerial conditions (Schipper et al. 2013a). While Schipper et al. (2013a) suggested strong shearing to be the dominant fragmentation mechanism for the Cordon Caulle particles, our results rather indicate a combination of shear (pre-)strain and thermal granulation to be responsible for the elongate tube Havre grains.

From all analysed experimental samples, PabrG was the only one that is grouped together with the natural angular ash samples (which have jagged shapes because of their vesicularity), sharing the same main cluster. This is probably a reflection of pre-fragmentation vesicularity. Pumice was the most abundant product of the 2012 eruption and it is very fragile (Jutzeler et al. 2014; Carey et al. 2018; Manga et al. 2018). On the other hand, it cannot be ignored that PabrG is also characterized by a measurable morphometric dissimilarity towards NatIang through NatIIIang. The slight but quantifiable morphometric difference could indicate that our "abrasion experiments" were overly simple, and that reproducing abrasive particles from pumice might require a more complex setup, such as a wave tank used by Jutzeler (2018). An even simpler explanation is that the pumice we abraded was from the seafloor, and thus had a different vesicle structure from raft pumice (Manga et al. 2018) that would be the most probable source of ash from abrasion.

In addition to revealing the generation mechanisms of the natural Havre ash, our results can also be used to study the influence of the three experimentally varied key parameters on particle formation and shape: fragmentation mechanism, melt material and post-fragmentation cooling history (determined by the sampling location).

While Figure 10 suggests that the fragmentation mechanism strongly affects the particles' morphometry, there are some notable exceptions. For example, RdryU is grouped separately from other samples generated by dry runs with dome rock (RdryG, RdryB, RdryW), and is surprisingly close to the IFCI samples RifciU and RifciW, separated by only a low dissimilarity value (see also Fig.9). This might indicate that RdryU samples, which were originally generated by "dry" overload of the melt plug experienced a different type of fragmentation, after having been splashed-down into water. This type of thermo-hydraulic mechanism might be similar to IFCI processes, but occurring on a microscopic scale, similar to the "secondary" magma-water interaction mechanisms, imposed on already-formed pyroclasts, discussed by Aravena et al. (2018).

The influence of material properties on particle shapes becomes evident when looking at the morphometric differences between RdryG and PdryG, which are relatively subtle but with t-tests detectable. Even more prominent is the morphometric difference between PgraM and RgraM, and between the samples RifciU/W and PifciU/W. All these sample pairs share the same fragmentation mechanism and post-fragmentation cooling history, yet they show clearly distinguishable morphometric features. These findings indicate a significant influence of pre-fragmentation melt material properties and suggest that it might be challenging to, for example, find a characteristic material-independent "morphometric signature" for IFCI processes. Currently there seem to be no feasible alternatives to material-specific lab experiments.

Our results show that the cooling history of particles significantly affects particle morphometry. This is especially evident in the comparison of RifciG and RifciB with RdryB and RdryG.

Due to the abundant presence of water during the fragmentation phase, the experimental IFCI fragments were most likely to have been in contact with water (and/or steam) at an early stage of ejection. The fragments from dry experiments did not experience such an early cooling effect and were therefore at higher temperature when entering the final stage of ballistic transport. The temperature gradient for "dry" fragments between being deposited into water (RdryB) and falling on the dry ground (RdryG) must have been considerably higher than for the “wet” IFCI fragments. We infer that grains of RdryB were affected by additional (secondary) thermal fragmentation processes after hitting the water. This would explain why RdryG and RdryB are significantly different in shape and even grouped in separate main clusters, whereas RifciG and RifciB are basically indistinguishable.

Our study's aim is to compare experimental grains with natural ones to infer fragmentation processes. Re-melting of crystal-poor Havre rock to produce analogue magma yields a crystal-poor melt-dominated mixture, and glassy particles. We intentionally compared experimental particles with glassy natural ones. This required exclusion of a relatively small proportion of natural particles (at most, fewer than 20%) from some sites, but we are confident that the remaining population is sufficient to represent natural particle morphology. An additional complication is that although we filtered out crystal-dominated particles based on SEM images during the segmentation step, we cannot know with this method whether micro-crystalline textures could be present inside the grains. We consider that this might have been the case for the Nat2 and Nat4 grains. As a consequence of this possible “contamination”, D_{max_cp} may have been overestimated, which would mean that e-tests would be less tightly constrained than with “uncontaminated” samples. The t-test and ANOVA results, however, showed no significant differences either among the natural curvi-planar samples (NatIcp - NatIVcp) or between them and the experimental samples RifciU and RifciW. The latter originated from a Havre re-melt with very low crystallinity. These results imply that “crystalline contamination” cannot have occurred on a major scale for these samples.

Finally, it has to be stressed that the 18 shape parameters used are certainly not statistically independent from each other. It is quite likely that some (or many) of these parameters are somewhat redundant, and add no, or only minor, morphometric information. Due to eq. (1) this might result in unbalanced weighing of some morphometric aspects on the dissimilarity. Comparative interpretations of dissimilarity values unequal to 0, in particular for cases where the differences between the dissimilarity values are small, should not be given too much weight. In such cases it might be arguable whether a slightly larger dissimilarity value really indicates a higher degree of morphometric difference. Importantly, however, this possible effect does not affect DAPM’s key output: identification of samples that are statistically equivalent morphometrically and separation of them from samples which are characterized by significant morphometric differences. Both types of findings (significant differences and statistical equivalence) are unaffected by the above mentioned potential redundancy effects. The use of all 18 parameters in this study serves mainly for demonstrating the potential of the DAPM. It leads to comprehensible clustering (Fig. 10) and promising results. Using a reduced set of shape parameters could further optimize the DAPM, if it can be ensured that the reduced set (i) effectively captures the nuances of morphometric dissimilarities, and (ii) the parameters are statistically independent from one another. While previous studies have suggested morphometric systems optimized for condition (i) (e.g., Dellino and La Volpe 1996; Liu et al. 2015b; Schmith et al. 2017), statistical independence is harder to achieve. One strategy could be to apply a principal component analysis (Davis 2002; in morphometric studies applied, e.g., by Maria and Carey 2002; Cioni et al. 2008; Schmith et al. 2017; Nurfiani and de Maisonneuve 2018) for a large set of shape parameters and use the resulting principle component scores as input parameters for DAPM.

Conclusions

With the dendrogrammatic analysis of particle morphometry (DAPM) we introduce a statistical tool for comparative particle shape analyses of multiple data sets. DAPM was designed to minimize statistical errors, sort the analyzed samples according to their morphometric dissimilarity, and identify samples of statistically equivalent shapes. We have demonstrated the utility of this method by applying it to the case study of the 2012 Havre eruption, in which we compared the particle shapes of eight natural ash samples with 14 samples from experiments that used re-melted Havre material to reproduce different fragmentation mechanisms under various post-fragmentation cooling conditions. Application of DAPM reveals that curvi-planar Havre ash originated from induced fuel-coolant interaction processes, while the elongate-tube ash probably resulted from syn-extrusive ash venting events. Furthermore, the influence of fragmentation mechanism, melt material properties and post-fragmentation cooling history on the particles' morphometry was explored. It is these dependencies that motivate the search for unique "global fingerprints" of certain fragmentation mechanisms.

While we used a set of 18 shape parameters provided by the 2D shape analyzing software PARTISAN (Dürig et al. 2018), the DAPM approach is not limited to this type of data. It can be applied for all sorts of data sets containing any morphometric descriptor in 2D or 3D.

Acknowledgements

Lisa Schmid, Rachael J. M. Baxter and Dylan Longridge are acknowledged for assisting with particle analysis. Louise Steffensen Schmidt is thanked for making Fig. 5. We thank Pierfrancesco Dellino, an anonymous reviewer, associate editor William W. Chadwick and executive editor Andrew J. L. Harris for their constructive comments, which helped improving our manuscript. This study was supported by MARSDEN grant U001616; Havre samples were obtained with NSF funding EAR1447559. T.D. is supported by the Icelandic Research Fund (Rannís) Grant Nr. 206527-051. R.J.C. was funded by Australian Research Council grants DP110102196 and DE150101190, and by US National Science Foundation grant OCE1357443.

Declarations

Note

This is a post-peer-review, pre-copyedit version of an article published in *Bulletin of Volcanology*. The final authenticated version is available online at: http://dx.doi.org/10.1007/s00445-020-01408-1

Funding

This study was supported by MARSDEN grant U001616; Havre samples were obtained with NSF funding EAR1447559.

Conflicts of interest/Competing interests

There are no competing interests

Availability of data and material

All data will be provided upon request to the lead author

Code availability

Not applicable

References

Ahad NA, Yahaya SSS (2014) Sensitivity analysis of Welch's t -test. In: AIP Conference Proceedings

Alvarado GE, Mele D, Dellino P, et al (2016) Are the ashes from the latest eruptions (2010–2016) at Turrialba volcano (Costa Rica) related to phreatic or phreatomagmatic events? J Volcanol Geotherm Res 327:407–415. https://doi.org/10.1016/j.jvolgeores.2016.09.003

Andronico D, Cristaldi A, Del Carlo P, Taddeucci J (2009) Shifting styles of basaltic explosive activity during the 2002–03 eruption of Mt. Etna, Italy. J Volcanol Geotherm Res 180:110–122. https://doi.org/10.1016/j.jvolgeores.2008.07.026

Aravena A, Vitturi M de M, Cioni R, Neri A (2018) Physical constraints for effective magma-water interaction along volcanic conduits during silicic explosive eruptions. Geology 46:867–870. https://doi.org/10.1130/G45065.1

Austin-Erickson A, Büttner R, Dellino P, et al (2008) Phreatomagmatic explosions of rhyolitic magma: Experimental and field evidence. J Geophys Res 113:B11201. https://doi.org/10.1029/2008JB005731

Avery MR, Panter KS, Gorsevski P V, et al (2017) Distinguishing styles of explosive eruptions at Erebus, Redoubt and Taupo volcanoes using multivariate analysis of ash morphometrics. J Volcanol Geotherm Res 332:1–13. https://doi.org/10.1016/j.jvolgeores.2017.01.010

Bender R, Lange S (2001) Adjusting for multiple testing—when and how? J Clin Epidemiol 54:343–349. https://doi.org/10.1016/S0895-4356(00)00314-0

Blanca MJ, Alarcón R, Arnau J, et al (2017) Non-normal data: Is ANOVA still a valid option? Psicothema 29:552–557. https://doi.org/10.7334/psicothema2016.383

Bonferroni CE (1936) Teoria statistica delle classi e calcolo delle probabilità. Pubbl del R Ist Super di Sci Econ e Commer di Firenze 8:3–62

Brosius F (1998) SPSS 8 Professionelle Statistik unter Windows. mitp-Verlag, Bonn

Büttner R, Dellino P, La Volpe L, et al (2002) Thermohydraulic explosions in phreatomagmatic eruptions as evidenced by the comparison between pyroclasts and products from Molten Fuel Coolant Interaction experiments. J Geophys Res Solid Earth 107:2277. https://doi.org/10.1029/2001JB000511

Büttner R, Dellino P, Raue H, et al (2006) Stress-induced brittle fragmentation of magmatic melts: Theory and experiments. J Geophys Res Solid Earth 111:1–10. https://doi.org/10.1029/2005JB003958

Büttner R, Dellino P, Zimanowski B (1999) Identifying magma-water interaction from the surface features of ash particles. Nature; London 401:688–690. https://doi.org/http://dx.doi.org.ezproxy.otago.ac.nz/10.1038/44364

Büttner R, Zimanowski B (1998) Physics of thermohydraulic explosions. Phys Rev E 57:5726–5729. https://doi.org/10.1103/PhysRevE.57.5726

Cannata CB, Rosa R De, Donato P, Taddeucci J (2014) Ash Features from Ordinary Activity at Stromboli Volcano. Int J Geosci 05:1361–1382. https://doi.org/10.4236/ijg.2014.511111

Carey R, Soule SA, Manga M, et al (2018) The largest deep-ocean silicic volcanic eruption of the past century. Sci Adv 4:e1701121. https://doi.org/10.1126/sciadv.1701121

Cas RAF, Giordano G (2014) Submarine Volcanism: a Review of the Constraints, Processes and Products, and Relevance to the Cabo de Gata Volcanic Succession. Ital J Geosci 133:362–377. https://doi.org/10.3301/IJG.2014.46

Cas RAF, Simmons JM (2018) Why Deep-Water Eruptions Are So Different From Subaerial Eruptions. Front Earth Sci 6:198. https://doi.org/10.3389/feart.2018.00198

Cashman K V, Scheu B (2015) Chapter 25 - Magmatic Fragmentation. In: Sigurdsson H (ed) The Encyclopedia of Volcanoes (Second Edition). Academic Press, Amsterdam, pp 459–471

Chadwick WW, Cashman K V., Embley RW, et al (2008) Direct video and hydrophone observations of submarine explosive eruptions at NW Rota-1 volcano, Mariana arc. J Geophys Res Solid Earth. https://doi.org/10.1029/2007JB005215

Cioni R, D'Oriano C, Bertagnini A (2008) Fingerprinting ash deposits of small scale eruptions by their physical and textural features. J Volcanol Geotherm Res 177:277–287. https://doi.org/10.1016/j.jvolgeores.2008.06.003

Cioni R, Pistolesi M, Bertagnini A, et al (2014) Insights into the dynamics and evolution of the 2010 Eyjafjallajökull summit eruption (Iceland) provided by volcanic ash textures. Earth Planet Sci Lett 394:111–123. https://doi.org/10.1016/j.epsl.2014.02.051

Coltelli M, Miraglia L, Scollo S (2008) Characterization of shape and terminal velocity of tephra particles erupted during the 2002 eruption of Etna volcano, Italy. Bull Volcanol 70:1103–1112. https://doi.org/10.1007/s00445-007-0192-8

Davis JC (2002) Statistics and Data Analysis in Geology, 3rd edition, 3rd edn. John Wiley & Sons, New York; Chichester; Brisbane

Dellino P, La Volpe L (1996) Image processing analysis in reconstructing fragmentation and transportation mechanisms of pyroclastic deposits. The case of Monte Pilato-Rocche Rosse eruptions, Lipari (Aeolian islands, Italy). J Volcanol Geotherm Res 71:13–29. https://doi.org/10.1016/0377-0273(95)00062-3

Dellino P, La Volpe L, Isaia R, Orsi G (2001) Statistical analysis of textural data from complex pyroclastic sequences: implications for fragmentation processes of the Agnano-Monte Spina Tephra (4.1 ka), Phlegraean Fields, southern Italy. Bull Volcanol 63:443–461. https://doi.org/10.1007/s004450100163

Dioguardi F, Mele D, Dellino P, Dürig T (2017) The terminal velocity of volcanic particles with shape obtained from 3D X-ray microtomography. J Volcanol Geotherm Res 329:41–53. https://doi.org/10.1016/j.jvolgeores.2016.11.013

Durant AJ, Rose WI, Sarna-Wojcicki AM, et al (2009) Hydrometeor-enhanced tephra sedimentation: Constraints from the 18 May 1980 eruption of Mount St. Helens. J Geophys Res 114:. https://doi.org/10.1029/2008JB005756

Dürig T, Bowman M, White J, et al (2018) PARTIcle Shape ANalyzer PARTISAN – an open source tool for multi-standard two-dimensional particle morphometry analysis. Ann Geophys 61:VO671. https://doi.org/10.4401/ag-7865

Dürig T, Dioguardi F, Büttner R, et al (2012a) A new method for the determination of the specific kinetic energy (SKE) released to pyroclastic particles at magmatic fragmentation: theory and first experimental results. Bull Volcanol 74:895–902. https://doi.org/10.1007/s00445-011-0574-9

Dürig T, Mele D, Dellino P, Zimanowski B (2012b) Comparative analyses of glass fragments from brittle fracture experiments and volcanic ash particles. Bull Volcanol 74:691–704. https://doi.org/10.1007/s00445-011-0562-0

Dürig T, Sonder I, Zimanowski B, et al (2012c) Generation of volcanic ash by basaltic volcanism. J Geophys Res Solid Earth 117:B01204. https://doi.org/10.1029/2011JB008628

Dürig T, White JDL, Murch AP, et al (2020) Deep-sea eruptions boosted by induced fuel–coolant explosions. Nat Geosci 13:498–503. https://doi.org/10.1038/s41561-020-0603-4

Dürig T, Zimanowski B (2012) "Breaking news" on the formation of volcanic ash: Fracture dynamics in silicate glass. Earth Planet Sci Lett 335:1–8. https://doi.org/10.1016/j.epsl.2012.05.001

Eychenne J, Houghton BF, Swanson DA, et al (2015) Dynamics of an open basaltic magma system: The 2008 activity of the Halemaʻumaʻu Overlook vent, Kīlauea

Caldera. Earth Planet Sci Lett 409:49–60. https://doi.org/10.1016/j.epsl.2014.10.045

Fauria KE, Manga M (2018) Pyroclast cooling and saturation in water. J Volcanol Geotherm Res. https://doi.org/10.1016/j.jvolgeores.2018.07.002

Fitch EP, Fagents SA (2020) Characteristics of rootless cone tephra emplaced by high-energy lava–water explosions. Bull Volcanol 82:62. https://doi.org/10.1007/s00445-020-01393-5

Games PA, Keselman HJ, Clinch JJ (1979) Tests for homogeneity of variance in factorial designs. Psychol Bull 86:978–984. https://doi.org/10.1037/0033-2909.86.5.978

Gilbert GK (1890) Lake Bonneville. U.S. Government Printing Office, Washington, D.C.

Gonnermann HM (2015) Magma Fragmentation. Annu Rev Earth Planet Sci 43:431–458. https://doi.org/10.1146/annurev-earth-060614-105206

Gurioli L, Andronico D, Bachelery P, et al (2015) MeMoVolc consensual document: a review of cross-disciplinary approaches to characterizing small explosive magmatic eruptions. Bull Volcanol 77:49. https://doi.org/10.1007/s00445-015-0935-x

Heiken G (1972) Morphology and petrography of volcanic ashes. Geol Soc Am Bull 83:1961–1988

Heiken G (1974) Atlas of Volcanic Ash. Smithson Contrib to Earth Sci 1–101. https://doi.org/10.5479/si.00810274.12.1

Heiken G, Wohletz K (1985) Volcanic ash. University of California Press, Berkeley

IBM Corp. (2017) IBM SPSS Statistics for Windows, Version 25.0. IBM Corp., Armonk, NY

Ikegami F, McPhie J, Carey R, et al (2018) The eruption of submarine rhyolite lavas and domes in the deep ocean – Havre 2012, Kermadec Arc. Front Earth Sci. https://doi.org/10.3389/feart.2018.00147

Iverson NA, Kyle PR, Dunbar NW, et al (2014) Eruptive history and magmatic stability of Erebus volcano, Antarctica: Insights from englacial tephra. Geochemistry, Geophys Geosystems 15:4180–4202. https://doi.org/10.1002/2014GC005435

Jordan SC, Dürig T, Cas RAF, Zimanowski B (2014) Processes controlling the shape of ash particles: Results of statistical IPA. J Volcanol Geotherm Res 288:19–27. https://doi.org/10.1016/j.jvolgeores.2014.09.012

Jutzeler M (2018) Products of Abrasion in Pumice Rafts: Wave Tank Experiments and Seafloor Samples. In: AGU Fall Meeting Abstracts. American Geophysical Union, Washington, pp V23F-0139

Jutzeler M, Marsh R, Carey RJ, et al (2014) On the fate of pumice rafts formed during the 2012 Havre submarine eruption. Nat Commun 5:3660. https://doi.org/10.1038/ncomms4660

Klawonn M, Frazer LN, Wolfe CJ, et al (2014) Constraining particle size-dependent plume sedimentation from the 17 June 1996 eruption of Ruapehu Volcano, New Zealand, using geophysical inversions. J Geophys Res Solid Earth 119:1749–1763.

https://doi.org/10.1002/2013JB010387
Lautze N, Taddeucci J, Andronico D, et al (2013) Insights into explosion dynamics and the production of ash at Stromboli from samples collected in real-time, October 2009. Geol Soc Am Spec Pap 498:125–139
Lautze NC, Taddeucci J, Andronico D, et al (2012) SEM-based methods for the analysis of basaltic ash from weak explosive activity at Etna in 2006 and the 2007 eruptive crisis at Stromboli. Phys Chem Earth, Parts A/B/C 45–46:113–127. https://doi.org/10.1016/j.pce.2011.02.001
Leibrandt S, Le Pennec J-L (2015) Towards fast and routine analyses of volcanic ash morphometry for eruption surveillance applications. J Volcanol Geotherm Res 297:11–27. https://doi.org/10.1016/j.jvolgeores.2015.03.014
Liu EJ, Cashman KV, Rust AC, Gislason SR (2015a) The role of bubbles in generating fine ash during hydromagmatic eruptions. Geology 43:239–242. https://doi.org/10.1130/G36336.1
Liu EJ, Cashman K V, Rust AC (2015b) Optimising shape analysis to quantify volcanic ash morphology. GeoResJ 8:14–30. https://doi.org/10.1016/j.grj.2015.09.001
Manga M, Fauria KE, Lin C, et al (2018) The pumice raft-forming 2012 Havre submarine eruption was effusive. Earth Planet Sci Lett 489:49–58. https://doi.org/10.1016/j.epsl.2018.02.025
Maria A, Carey S (2007) Quantitative discrimination of magma fragmentation and pyroclastic transport processes using the fractal spectrum technique. J Volcanol Geotherm Res 161:234–246. https://doi.org/10.1016/j.jvolgeores.2006.12.006
Maria A, Carey S (2002) Using fractal analysis to quantitatively characterize the shapes of volcanic particles. J Geophys Res Solid Earth 107:ECV 7-1-ECV 7-17. https://doi.org/10.1029/2001JB000822
Mele D, Dellino P, Sulpizio R, Braia G (2011) A systematic investigation on the aerodynamics of ash particles. J Volcanol Geotherm Res 203:1–11. https://doi.org/10.1016/j.jvolgeores.2011.04.004
Mele D, Dioguardi F, Dellino P, et al (2015) Hazard of pyroclastic density currents at the Campi Flegrei Caldera (Southern Italy) as deduced from the combined use of facies architecture, physical modeling and statistics of the impact parameters. J Volcanol Geotherm Res 299:35–53. https://doi.org/10.1016/j.jvolgeores.2015.04.002
Miwa T, Geshi N, Shinohara H (2013) Temporal variation in volcanic ash texture during a vulcanian eruption at the Sakurajima volcano, Japan. J Volcanol Geotherm Res 260:80–89. https://doi.org/10.1016/j.jvolgeores.2013.05.010
Miwa T, Shimano T, Nishimura T (2015) Characterization of the luminance and shape of ash particles at Sakurajima volcano, Japan, using CCD camera images. Bull Volcanol 77:5. https://doi.org/10.1007/s00445-014-0886-7
Murch AP, White JDL, Barreyre T, et al (2020) Volcaniclastic Dispersal During Submarine Lava Effusion: The 2012 Eruption of Havre Volcano, Kermadec Arc, New Zealand. Front Earth Sci. https://doi.org/10.3389/feart.2020.00237

Murch AP, White JDL, Carey RJ (2019a) Unusual fluidal behavior of a silicic magma during fragmentation in a deep subaqueous eruption, Havre volcano, southwestern Pacific Ocean. Geology. https://doi.org/10.1130/G45657.1

Murch AP, White JDL, Carey RJ (2019b) Characteristics and Deposit Stratigraphy of Submarine-Erupted Silicic Ash, Havre Volcano, Kermadec Arc, New Zealand. Front Earth Sci 7:1–21. https://doi.org/10.3389/feart.2019.00001

Murtagh RM, White JDL (2013) Pyroclast characteristics of a subaqueous to emergent Surtseyan eruption, Black Point volcano, California. J Volcanol Geotherm Res 267:75–91. https://doi.org/10.1016/j.jvolgeores.2013.08.015

Nelson WA (2008) Statistical Methods. In: Encyclopedia of Ecology, Five-Volume Set

Nurfiani D, de Maisonneuve CB (2018) Furthering the investigation of eruption styles through quantitative shape analyses of volcanic ash particles. J Volcanol Geotherm Res 354:102–114

Papale P (1999) Strain-induced magma fragmentation in explosive eruptions. Nature 397:425–428. https://doi.org/10.1038/17109

Perneger T V (1998) What's wrong with Bonferroni adjustments. BMJ 316:1236–1238. https://doi.org/10.1136/bmj.316.7139.1236

Rasch D, Guiard V (2004) The robustness of parametric statistical methods. Psychol Sci

Riley CM, Rose WI, Bluth GJS (2003) Quantitative shape measurements of distal volcanic ash. J Geophys Res Solid Earth 108:. https://doi.org/10.1029/2001JB000818

Schipper CI, Castro JM, Tuffen H, et al (2013a) Shallow vent architecture during hybrid explosive–effusive activity at Cordón Caulle (Chile, 2011–12): evidence from direct observations and pyroclast textures. J Volcanol Geotherm Res 262:25–37

Schipper CI, Sonder I, Schmid A, et al (2013b) Vapour dynamics during magma–water interaction experiments: hydromagmatic origins of submarine volcaniclastic particles (limu o Pele). Geophys J Int 192:1109–1115. https://doi.org/10.1093/gji/ggs099

Schmith J, Höskuldsson Á, Holm PM (2017) Grain shape of basaltic ash populations: implications for fragmentation. Bull Volcanol 79:14. https://doi.org/10.1007/s00445-016-1093-5

Scrope GJ (1858) The Geology and Extinct Volcanoes of Central France. John Murray, London

Student (1908) The Probable Error of a Mean. Biometrika 6:. https://doi.org/10.2307/2331554

Suzuki Y, Nagai M, Maeno F, et al (2013) Precursory activity and evolution of the 2011 eruption of Shinmoe-dake in Kirishima volcano—insights from ash samples. Earth, Planets Sp 65:591–607. https://doi.org/10.5047/eps.2013.02.004

Taddeucci J, Palladino D (2002) Particle size-density relationships in pyroclastic deposits: inferences for emplacement processes. Bull Volcanol 64:273–284. https://doi.org/10.1007/s00445-002-0205-6

Tukey JW (1949) Comparing individual means in the analysis of variance. Biometrics 5:99–114

van Otterloo J, Cas RAF, Scutter CR (2015) The fracture behaviour of volcanic glass and relevance to quench fragmentation during formation of hyaloclastite and phreatomagmatism. Earth-Science Rev.

Verolino A, White JDL, Dürig T, Cappuccio F (2019) Black Point – Pyroclasts of a Surtseyan eruption show no change during edifice growth to the surface from 100 m water depth. J Volcanol Geotherm Res 384:85–102. https://doi.org/10.1016/j.jvolgeores.2019.07.013

Walker E, Nowacki AS (2011) Understanding equivalence and noninferiority testing. J Gen Intern Med 26:192–196. https://doi.org/10.1007/s11606-010-1513-8

Welch BL (1947) The Generalization of `Student's' Problem when Several Different Population Variances are Involved. Biometrika 34:28–35. https://doi.org/10.2307/2332510

Wellek S (2010) Testing Statistical Hypotheses of Equivalence and Noninferiority. Chapman and Hall/CRC

White JDL (2000) Subaqueous eruption-fed density currents and their deposits. Precambrian Res 101:87–109. https://doi.org/10.1016/S0301-9268(99)00096-0

White JDL, McPhie J, Soule SA (2015) Chapter 19 - Submarine Lavas and Hyaloclastite. In: Sigurdsson H (ed) The Encyclopedia of Volcanoes (Second Edition). Academic Press, Amsterdam, pp 363–375

White JDL, Valentine GA (2016) Magmatic versus phreatomagmatic fragmentation: Absence of evidence is not evidence of absence. Geosphere 12:1478–1488. https://doi.org/10.1130/GES01337.1

Wohletz KH (1986) Explosive magma-water interactions: Thermodynamics, explosion mechanisms, and field studies. Bull Volcanol 48:245–264. https://doi.org/10.1007/BF01081754

Wohletz KH, Zimanowski B, Büttner R (2013) Magma-water interactions. In: Fagents SA, Gregg TKP, Lopes RMC (eds) Modeling Volcanic Processes: The Physics and Mathematics of Volcanism. Cambridge University Press, Cambridge, pp 230–257

Wright HMN, Cashman K V, Mothes PA, et al (2012) Estimating rates of decompression from textures of erupted ash particles produced by 1999-2006 eruptions of Tungurahua volcano, Ecuador. Geology 40:619–622. https://doi.org/10.1130/G32948.1

Yamanoi Y, Takeuchi S, Okumura S, et al (2008) Color measurements of volcanic ash deposits from three different styles of summit activity at Sakurajima volcano, Japan: Conduit processes recorded in color of volcanic ash. J Volcanol Geotherm Res 178:81–93. https://doi.org/10.1016/j.jvolgeores.2007.11.013

Zabell SL (2008) On Student's 1908 article "the probable error of a mean." J Am Stat Assoc. https://doi.org/10.1198/016214508000000030

Zhang Y (1999) A criterion for the fragmentation of bubbly magma based on brittle failure theory. Nature 402:648–650. https://doi.org/10.1038/45210

Zimanowski B, Büttner R, Dellino P, et al (2015) Magma–Water Interaction and Phreatomagmatic Fragmentation. In: The Encyclopedia of Volcanoes. Elsevier, pp 473–484

Zimanowski B, Wohletz K, Dellino P, Büttner R (2003) The volcanic ash problem. J Volcanol Geotherm Res 122:1–5

Table 1: Number of glassy ash particles by morphological class, following the classification of Murch et al. (2019b). Values in brackets show percentages. Sample subsets marked by asterisk were used for the determination of D_{max_cp} and D_{max_ang}.

	Curvi-planar	angular	elongate-tube	fluidal
Nat1	74 (51.7%)*	28 (19.6%)*	25 (17.5%)	16 (11.2%)
Nat2	17 (42.5%)	13 (32.5%)	9 (22.5%)	1 (2.5%)
Nat3	28 (66.7%)*	6 (14.3%)	7 (16.7%)	1 (2.4%)
Nat4	35 (36.5%)*	55 (57.3%)*	3 (3.1%)	3 (3.1%)
Nat5	55 (51.4%)*	41 (38.3%)*	8 (7.5%)	3 (2.8%)
Nat6	38 (56.7%)*	20 (29.9%)*	7 (10.4%)	2 (3.0%)
	247 (49.9%)	163 (32.9%)	59 (11.9%)	26 (5.3%)

Table 2: Shape parameters used for morphometric analysis. It is to note that various parameters of identical names (e.g. "convexity") are differently defined within the different systems. For the mathematical definitions of each parameter, we refer to the reader to the cited sources and to Table 2 in Dürig et al. (2018). In addition, the equivalence margins are listed for curvi-planar (D_{max_cp}) and for angular particles (D_{max_ang}). These values serve as threshold values when applying equivalence tests.

label	shape parameter	D_{max_cp}	D_{max_ang}	morphometric system by
Circ_DL	circularity	0.13	0.14	Dellino and La Volpe (1996)
Rec_DL	rectangularity	0.07	0.08	
Com_DL	compactness	0.06	0.06	
Elo_DL	elongation	0.53	0.49	
Circ_CI	circularity	0.12	0.12	Cioni et al. (2014)
AR_CI	aspect ratio	0.45	0.38	
Con_CI	convexity	0.07	0.07	
Sol_CI	solidity	0.10	0.07	
Circ_LL	circularity	0.08	0.08	Leibrandt and Le Pennec (2015)
Elo_LL	elongation	0.12	0.12	
AR_LL	aspect ratio	0.12	0.12	
Con_LL	convexity	0.06	0.07	
FF	form factor	0.12	0.12	Liu et al. (2015b)
AR_LI	convexity	0.14	0.14	
Circ_SC	circularity	0.12	0.12	Schmith et al. (2017)
AR_F	Feret aspect ratio	0.16	0.13	
AR_SC	reciprocal aspect ratio	0.37	0.30	
Reg	regularity	0.11	0.12	

Table 3: Results of e-tests. Sample sizes are presented as N1 and N2. Test values *D* represent the minimum equivalence margin, under which an e-test would still be passed. For the presented tests we used both D_{max_cp} and D_{max_ang} as threshold values. If *D* is equal or smaller than the given threshold values, a statistical equivalence of the tested data sets is verified ("yes" in the columns labelled "stat eqv"). F-tests were used to test the variances of the data sets for homogeneity, which is a necessary pre-condition for a valid e-test. In cases where this pre-condition was not met, no statement can be made, in the table indicated by "(?)". The bottom row shows the number of parameters, for which a statistical equivalence was verified.

data 1			NatItub		RifciG		PifciW	
data 2			RgraM		RifciB		PifciU	
	D_{max_cp}	D_{max_ang}	*D*	stat eqv	*D*	stat eqv	*D*	stat eqv
N1			61		46		66	
N2			74		59		38	
Circ_DL	0.13	0.14	0.06	yes	0.06	yes	(?)	(?)
Rec_DL	0.07	0.08	0.04	yes	0.03	yes	0.03	yes
Com_DL	0.06	0.06	0.04	yes	0.04	yes	0.07	yes
Elo_DL	0.53	0.49	0.32	yes	0.41	yes	(?)	(?)
Circ_CI	0.12	0.12	0.04	yes	0.05	yes	0.10	yes
AR_CI	0.45	0.38	0.25	yes	0.23	yes	(?)	(?)
Con_CI	0.07	0.07	0.04	yes	0.04	yes	0.03	yes
Sol_CI	0.10	0.07	0.03	yes	0.05	yes	(?)	(?)
Circ_LL	0.08	0.08	0.03	yes	0.04	yes	0.07	yes
Elo_LL	0.12	0.12	0.07	yes	(?)	(?)	0.13	yes
AR_LL	0.12	0.12	0.07	yes	(?)	(?)	0.13	yes
Con_LL	0.06	0.07	0.04	yes	0.03	yes	0.03	yes
FF	0.12	0.12	0.04	yes	0.05	yes	0.10	yes
AR_LI	0.14	0.14	0.07	yes	0.06	yes	0.12	yes
Circ_SC	0.12	0.12	0.06	yes	(?)	(?)	0.12	yes
AR_F	0.16	0.13	0.07	yes	0.07	yes	0.14	yes
AR_SC	0.37	0.30	0.25	yes	0.25	yes	(?)	(?)
Reg	0.11	0.12	0.04	yes	(?)	(?)	0.08	yes
equivalent parameters			18/18		14/18		13/18	

Table 4 Results of two-tailed t-tests. Given values represent *p*-values in percent for cases of verified significant differences. Cases for which no significant difference was found (i.e., where $p > 5\%$) are indicated by “-“. N1 and N2 denote sample sizes.

data 1	**RifciG**	**RifciB**	**RdryG**	**RifciW**	**RifciU**
data 2	**PifciW**	**PifciU**	**PdryG**	**NatIcp**	**NatIIcp**
	t-test	**t-test**	**t-test**	**t-test**	**t-test**
N1	46	59	43	66	57
N2	66	38	54	56	51
Circ_DL	-	-	3.0	-	-
Rec_DL	-	-	2.8	-	-
Com_DL	-	0.9	-	-	-
Elo_DL	-	-	-	-	-
Circ_CI	-	-	1.1	-	-
AR_CI	3.4	-	-	-	-
Con_CI	-	-	1.4	-	-
Sol_CI	-	4.0	2.8	-	-
Circ_LL	-	-	1.1	-	-
Elo_LL	-	-	-	-	-
AR_LL	-	-	-	-	-
Con_LL	-	-	-	-	-
FF	-	-	1.1	-	-
AR_LI	-	-	-	-	-
Circ_SC	-	-	-	-	-
AR_F	-	-	-	-	-
AR_SC	-	-	-	-	-
Reg	-	-	-	-	-

Table 5 Results of e-tests verifying statistical equivalence between the morphometric characteristics of curvi-planar ash, RifciU and RifciW samples. Sample sizes are presented as N1 and N2. Test values D represent the minimum equivalence margin, under which an e-test would still be passed. F-tests were used to test the variances of the data sets for homogeneity, which is a necessary pre-condition for a valid e-test. When this pre-condition was not met, the results were ignored (indicated by "(?)"). If D is equal or smaller than the threshold D_{max_cp}, a statistical equivalence of the tested data sets is verified ("yes" in the columns labelled "stat eqv"). E-tests with RifciU showed no complete set of test values for any of the natural ash samples, therefore the maxima of all valid D values was computed (presented in the column "D_{max}") and used for comparison with D_{max_cp}.

data 1		**RifciU**	**RifciU**	**RifciU**	**RifciU**	**RifciU**		**RifciW**	
data 2		**NatIcp**	**NatIIcp**	**NatIIIcp**	**NatIVcp**	**NatIcp - NatIVcp**		**NatIVcp**	
	D_{max_cp}	D	D	D	D	D_{max}	**stat eqv**		**stat eqv**
N1		57	57	57	57	57		66	
N2		56	51	79	61	247		56	
Circ_DL	0.13	0.05	0.05	0.04	0.07	0.07	yes	0.05	yes
Rec_DL	0.07	(?)	0.02	0.03	0.03	0.03	yes	0.03	yes
Com_DL	0.06	0.04	0.03	(?)	(?)	0.04	yes	0.03	yes
Elo_DL	0.53	(?)	(?)	(?)	0.33	0.33	yes	0.38	yes
Circ_CI	0.12	0.04	0.04	0.03	0.06	0.06	yes	0.04	yes
AR_CI	0.45	(?)	(?)	0.17	0.23	0.23	yes	0.23	yes
Con_CI	0.07	(?)	0.04	0.04	0.04	0.04	yes	0.02	yes
Sol_CI	0.10	(?)	0.02	(?)	(?)	0.02	yes	0.02	yes
Circ_LL	0.08	0.03	0.03	0.02	0.04	0.04	yes	0.03	yes
Elo_LL	0.12	0.09	(?)	0.05	0.09	0.09	yes	0.07	yes
AR_LL	0.12	0.09	(?)	0.05	0.09	0.09	yes	0.07	yes
Con_LL	0.06	(?)	0.03	0.03	0.02	0.03	yes	0.02	yes
FF	0.12	0.04	0.04	0.03	0.06	0.06	yes	0.04	yes
AR_LI	0.14	0.08	(?)	0.05	0.09	0.09	yes	0.08	yes
Circ_SC	0.12	(?)	(?)	0.05	0.09	0.09	yes	0.05	yes
AR_F	0.16	0.09	(?)	0.06	0.11	0.11	yes	0.08	yes
AR_SC	0.37	(?)	(?)	0.16	0.24	0.24	yes	0.23	yes
Reg	0.11	0.04	0.06	0.03	0.07	0.07	yes	0.04	yes

Fig. 1 Map of Havre volcano and sample locations. The bathymetric changes during the 2012 eruption are colorized (Carey et al. 2018). The natural ash samples Nat1 – Nat6 were retrieved at various locations around the caldera, marked by yellow circles. The sites where pieces of giant pumice and dome rock were retrieved are marked with “P” and “R”, respectively.

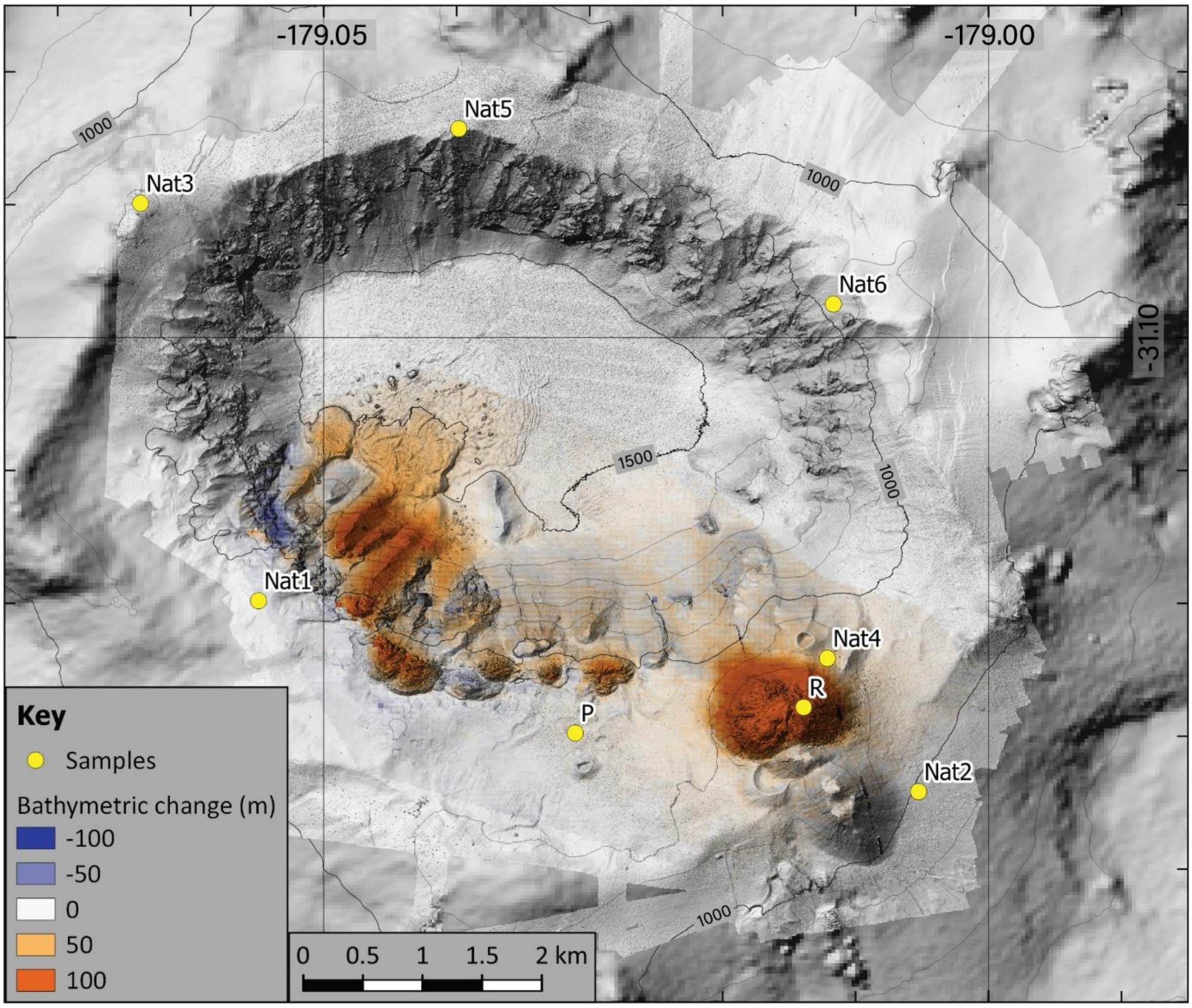

Fig. 2 SEM images of representative Havre ash particles sorted by the three morphological classes analyzed in this study. The top row depicts curvi-planar grains from NatIcp (a), NatIIcp (b), NatIIIcp (c) and NatIVcp (d). The middle row shows angular grains from NatIang (e, f), NatIIang (g) and NatIIIang (h), while elongate-tube grains from NatItub (i-l) are presented in the bottom row. White scale bars correspond to 50 µm.

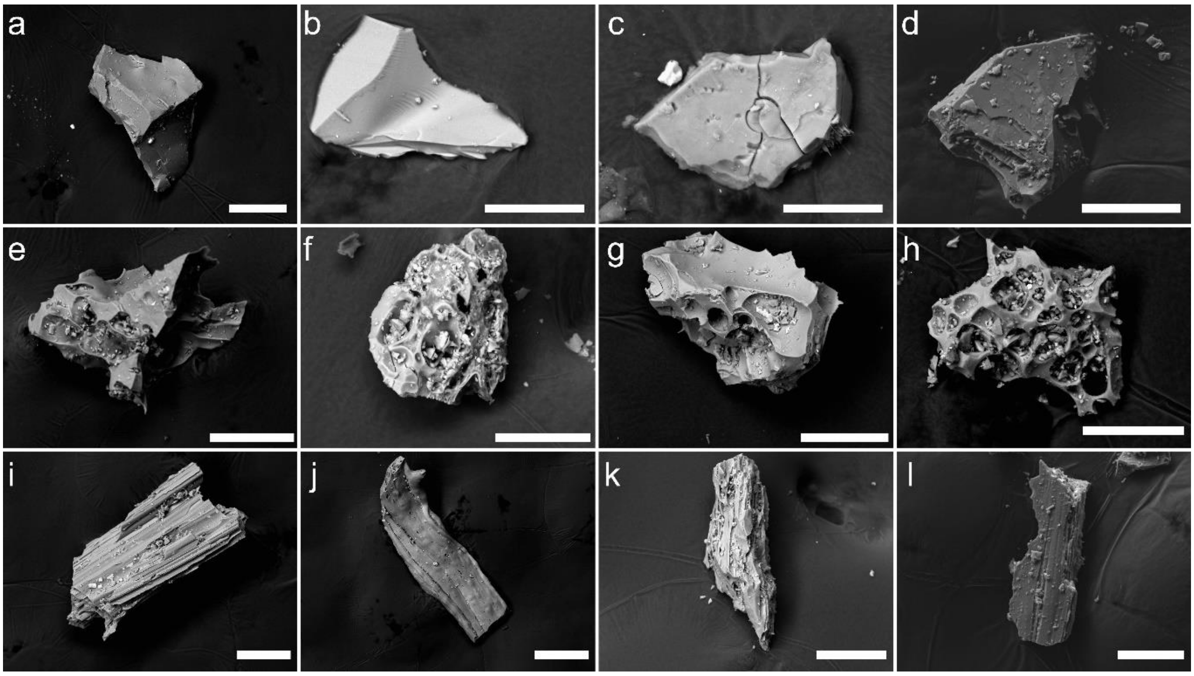

Fig 3 SEM images of representative experimental grains. Two images are presented for each experimental sample: PabrG (a, b), PdryG (c, d), PgraM (e, f), PifciU (g, h), PifciW (i, j), RconC (k, l), RdryB (m, n), RdryG (o, p), RdryU (q, r), RgraM (s, t), RifciB (u, v), RifciG (w, x), RifciU (y, z), RifciW (A, B). White scale bars correspond to 50 µm.

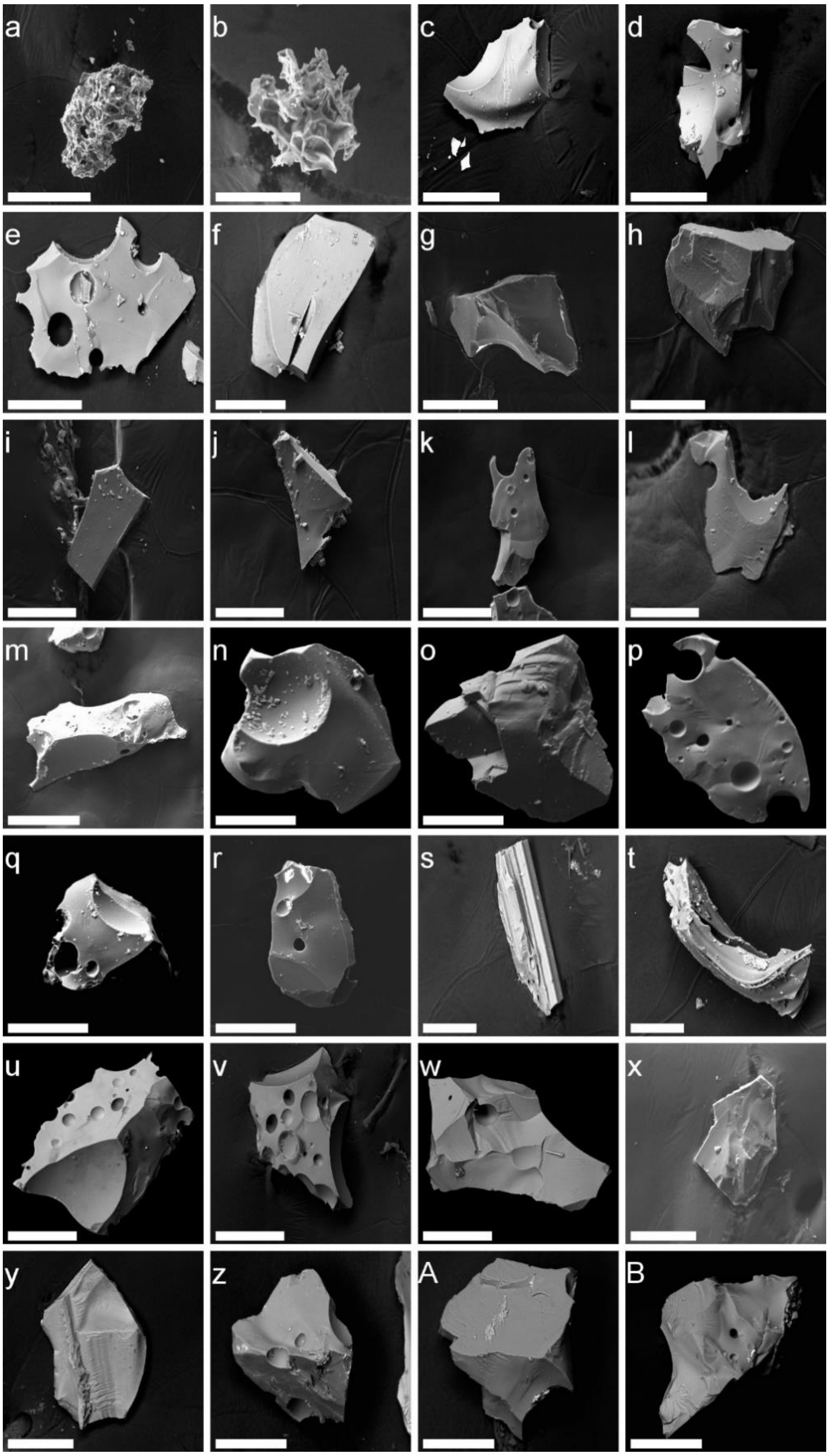

Fig. 4 Illustrated notation system for natural ash and experimental particle samples. This figure serves also as legend for Fig. 10. a. The label of natural ash samples is composed of the identifier “Nat”, followed by a roman number and a label indicating the morphological class. (For example, “NatIIIcp” stands for the third of the randomly selected sample set from the binned curvi-planar ash grains.) b. Experimental samples are denoted by a combination of indicators, representing the starting material, type of experiment and location of particle sampling. c. Exemplary demonstration for the use of this systematic.

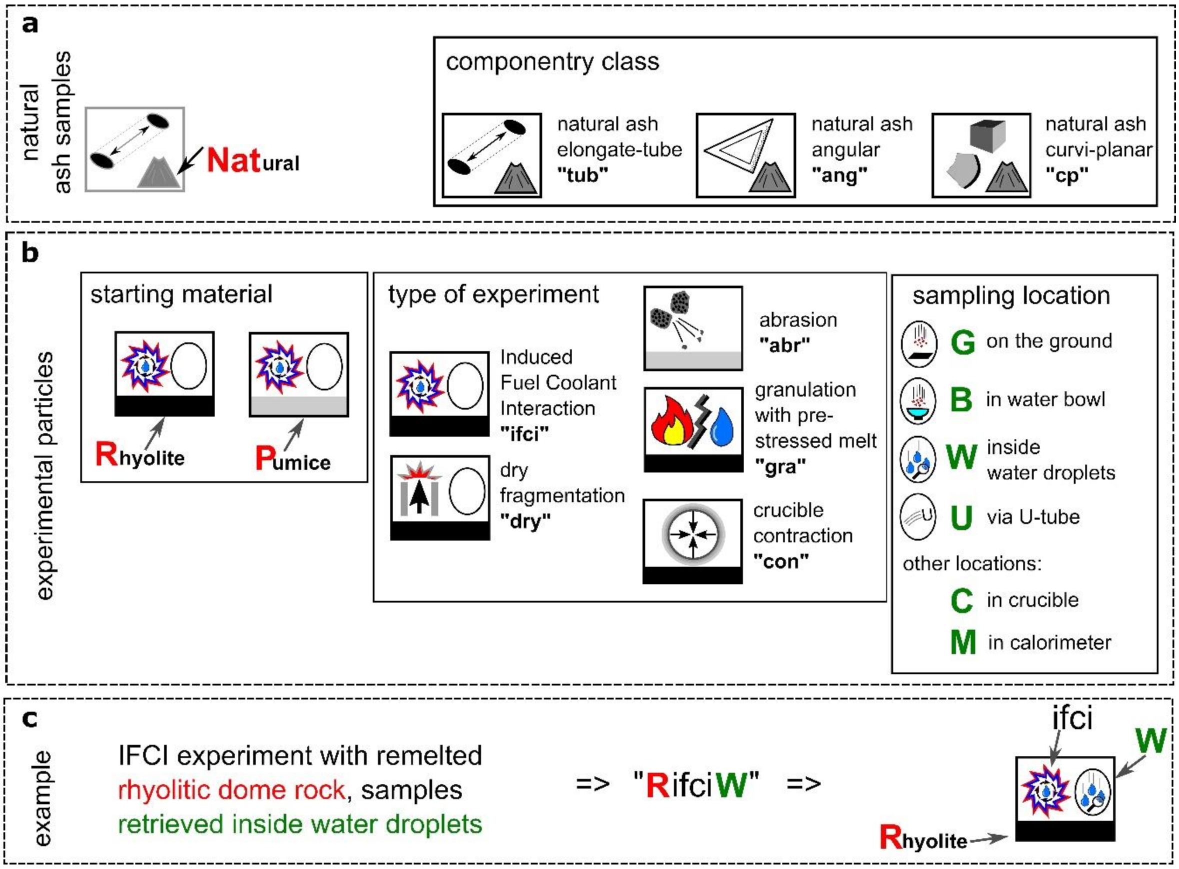

Fig. 5 Example for the binarization and morphometric characterization of a particle. In the depicted case, the SEM image shows a particle from sample RifciU (a) that was binarized, resulting in a silhouette image (b). Based on such binary images, 18 shape parameters were computed by means of the software PARTISAN (see Table 2), leading to a morphometric profile for each particle (c).

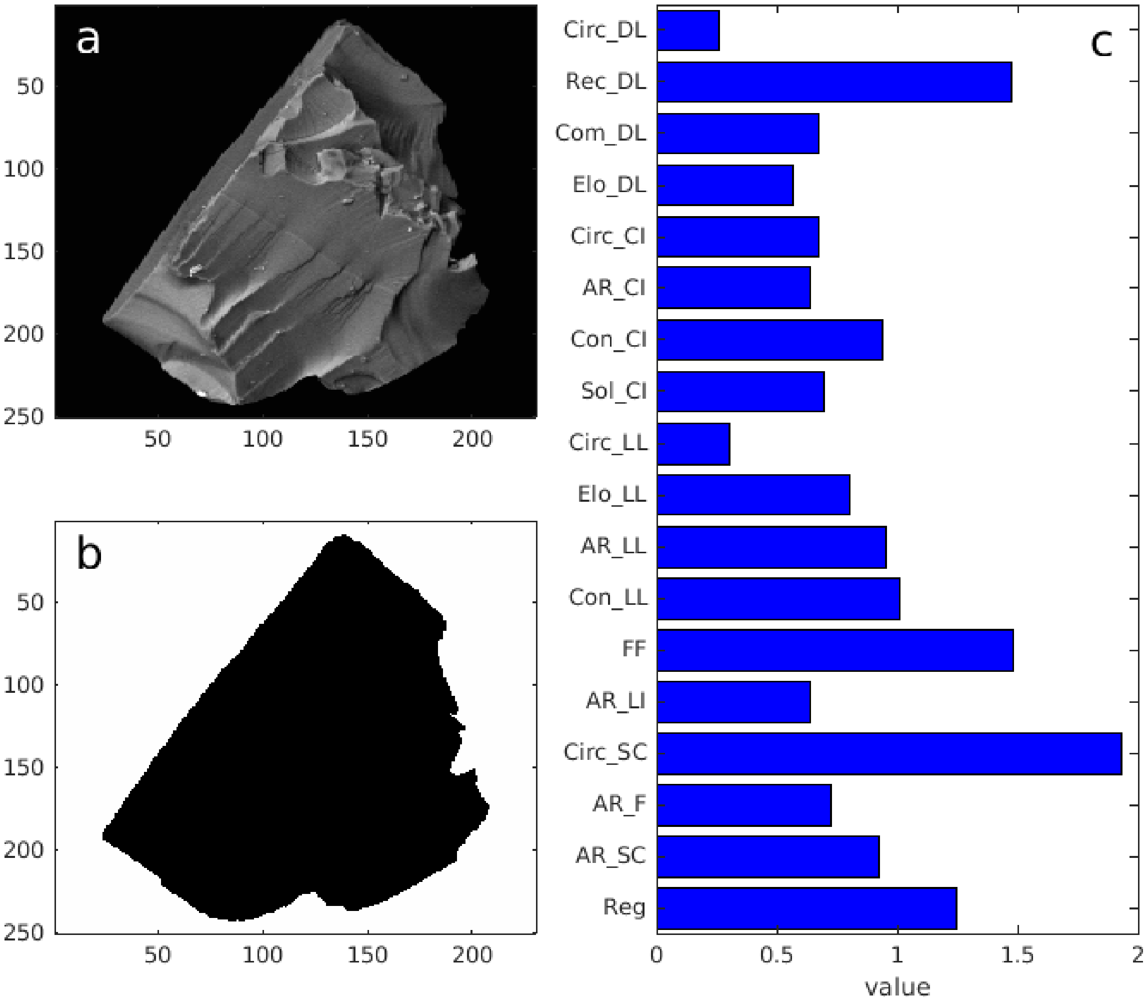

Fig. 6 “Level 1” dendrogram. This dendrogram is based on one-way ANOVA with all 22 data sets and subsequent computation of the distance matrix X by equation (1). Four main clusters of samples with relatively similar shape parameters can be identified.

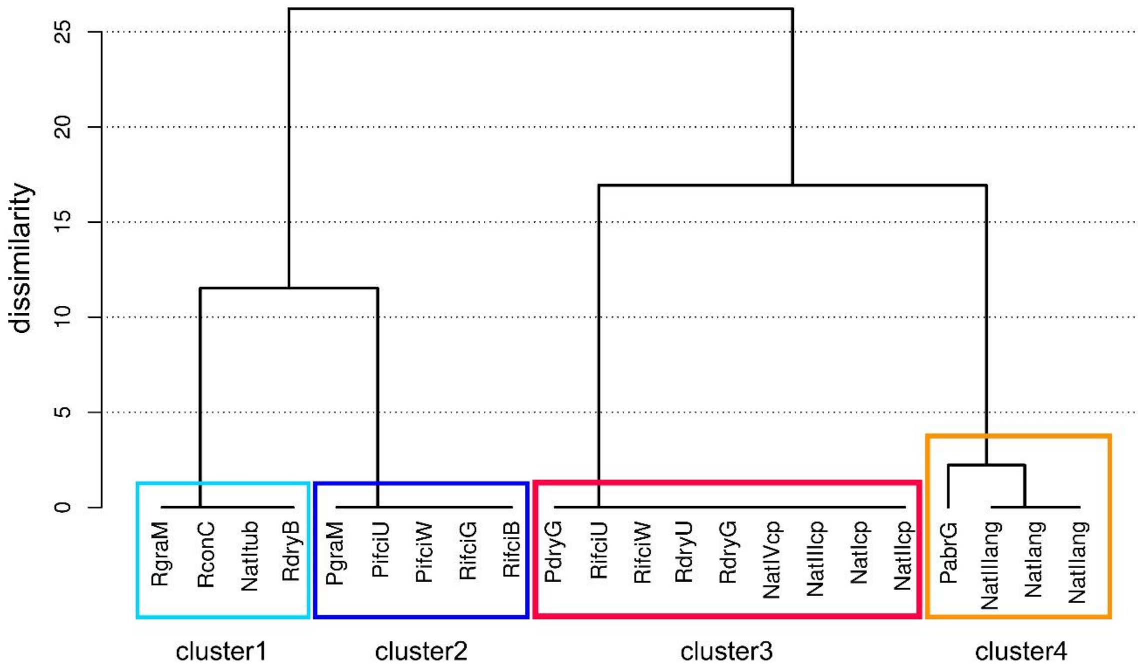

Fig. 7 “Level 2” dendrogram of cluster1. NatItub and RgraM are statistically equivalent, which was verified by additional t- and e-tests. Thus, granulation experiments with pre-stressed remelted dome rock reproduced fragments of comparable morphometric characteristics to the elongate-tube ash particles retrieved on the sea floor.

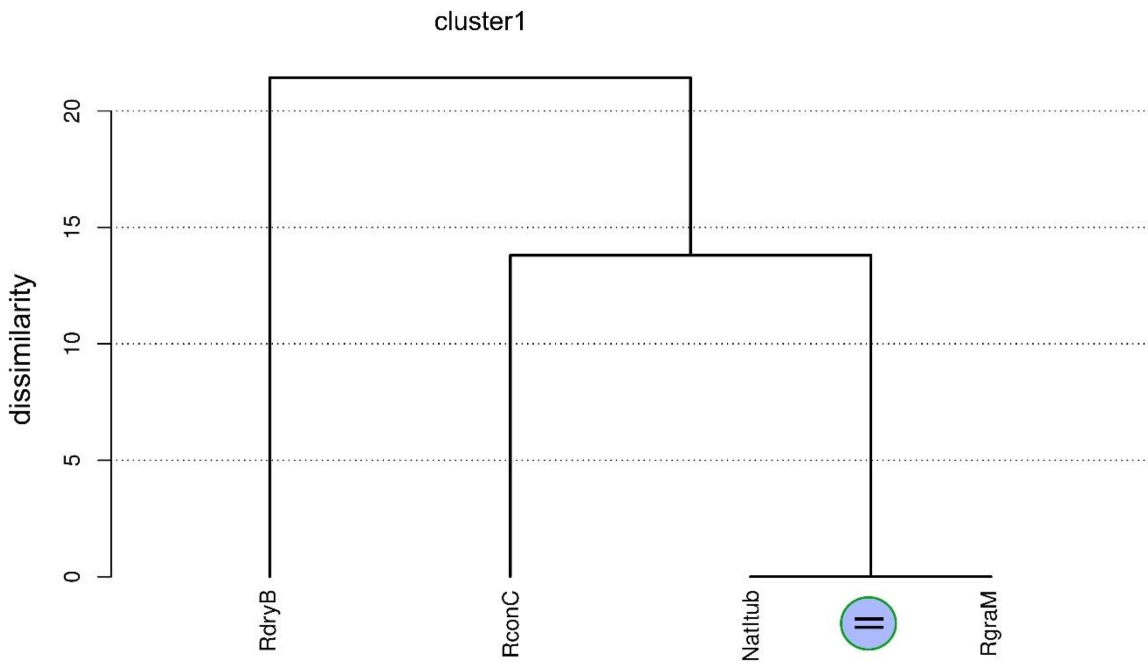

Fig. 8 “Level 2” dendrogram of cluster2. According to the ANOVA PgraM is clearly distinguishable from the other samples. While they appear to be grouped together, further t-tests and e-tests suggest a further separation between PifciU/W and RifciG/W.

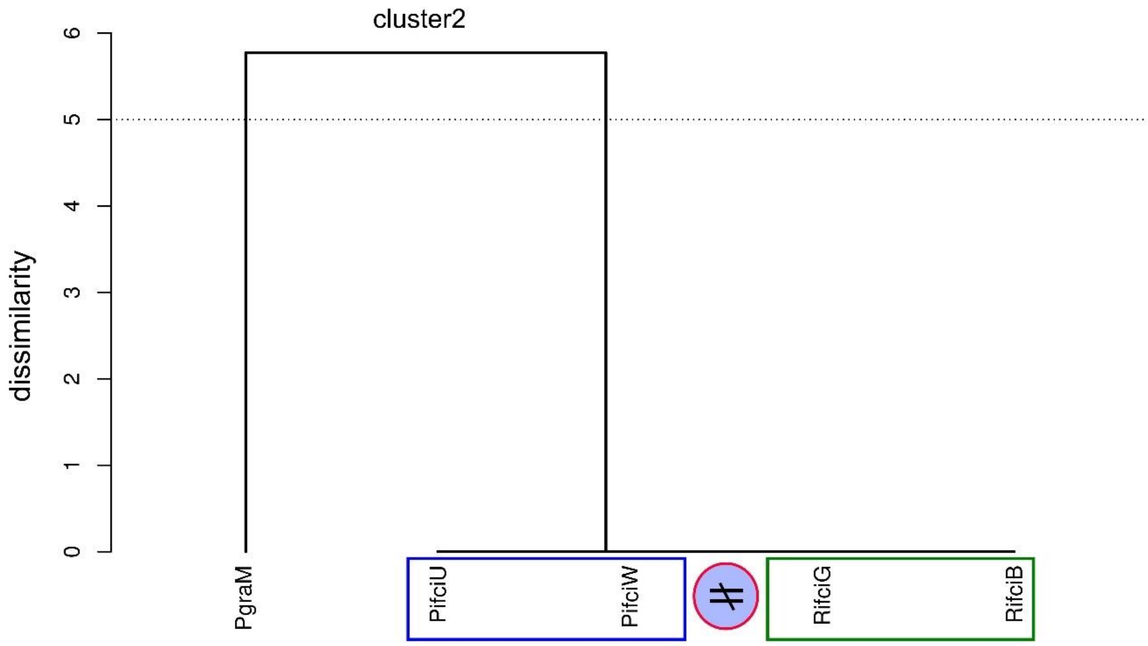

Fig. 9 “Level 2” dendrogram of cluster 3. The samples which appeared to be similar in the “level 1” dendrogram are now divided into three sub-groups. While t-tests show significant differences between RdryG and PdryG in one sub-group, no such differences could be found for the members of the biggest sub-group. In fact, e-tests verify that experimental samples RifciU and RifciW are statistically equivalent with the natural curvi-planar ash samples NatIcp – NatIVcp.

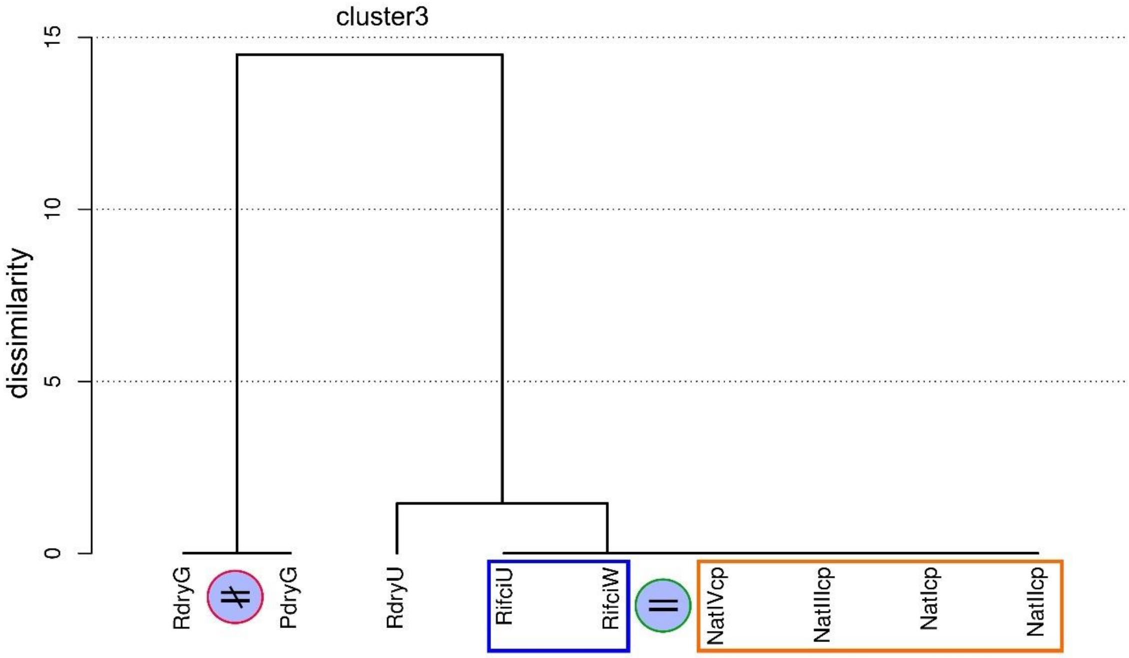

Fig. 10 Overview of the results from DAPM. The fan dendrogram illustrates the merged findings from “level 1” and “level 2” dendrograms, t-tests and e-tests. Samples characterized by statistical equivalence in all morphometric parameters are indicated by identical color in branch, label and icon frame. A legend for the icons is provided in Fig. 4.